RSC Advances

ROYAL SOCIETY OF CHEMISTRY

www.rsc.org/advances

Graphical Abstract

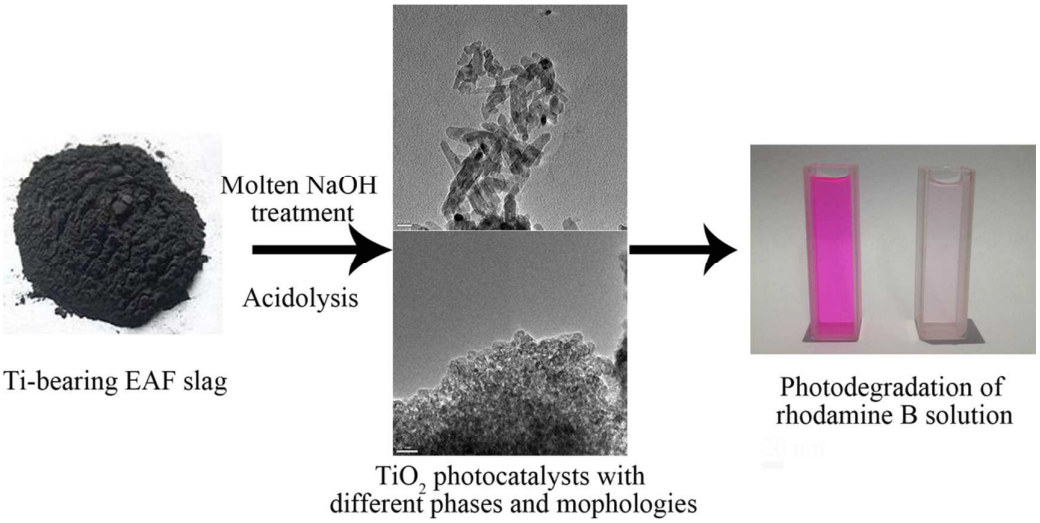

TiO_2 photocatalysts with different crystal phases and morphologies were synthesized from Ti-bearing EAF slag.

Journal Name RSCPublishing

ARTICLE

Cite this: DOI: 10.1039/x0xx00000x

Received 00th January 2012,
Accepted 00th January 2012

DOI: 10.1039/x0xx00000x

www.rsc.org/

Influence of acid type and concentration on the synthesis of nanostructured titanium dioxide photocatalyst from titanium-bearing electric arc furnace molten slag

Yang Li, Yang Yang, Min Guo* and Mei Zhang

In this paper, nanostructured titanium dioxide (TiO_2) photocatalysts with different crystal structures and morphologies were successfully synthesized from titanium-bearing electric arc furnace molten slag (Ti-bearing EAF slag). The effects of different kinds of acid and acid concentrations during the acidolysis process on the crystal structures and morphologies of TiO_2 were systematically studied. And the TiO_2 crystal phase transformation mechanism and morphology evolution in different acid systems and concentrations were discussed in detail. In addition, the photocatalytic properties of TiO_2 obtained in different acid systems were investigated. It is shown that rutile and anatase type TiO_2 were obtained in hydrochloric acid and sulfuric acid, respectively, while two types coexisted in nitric acid. With increasing sulfuric acid concentration, anatase would be apt to change to rutile. The growth mechanism of TiO_2 from Ti-bearing EAF slag was also discussed. The TiO_2 synthesized from sulfuric acid showed better photocatalytic activity than that from hydrochloric or nitric acid, and its photodegradation efficiency can reach 90.52% in 90 min for rhodamine B solution.

* School of Metallurgical and Ecological Engineering, University of Science and Technology Beijing, Beijing 100083, P. R. China. E-mail: guomin@ustb.edu.cn; Tel: +86-010-62334926

Journal Name RSCPublishing

ARTICLE

1. Introduction

TiO_2 is an important semiconductor material used in various fields such as coatings [1], fillers for plastic and paper, photocatalysts [2, 3], gas sensors [4] and solar energy conversion materials [5, 6]. Owing to its relatively high redox potential, chemical stability and nontoxic nature, TiO_2 has been regard as one of the best photocatalyst for many years [3], and its photocatalytic property strongly depends on crystalline phase and micromorphology. Till now, various methods had been developed to prepare nano TiO_2 with different morphologies (size, shape, etc.) and crystalline phases by using pure chemical reagents [7-9]. For instance, Wu et al. [10] proposed a sol-hydrothermal method to synthesize pure anatase or rutile type TiO_2 nanocrystals with uniform size by titanium *n*-butoxide in various acidic mediums. They found that the acid type such as HCl, HNO_3, H_2SO_4, and CH_3COOH had significant influence on the crystalline phase of obtained nanoparticles. Rajesh et al. [11] also studied the effects of acid species and concentration on the obtained TiO_2 particles from $TiCl_4$ by direct thermal hydrolysis approach. It was shown that the samples synthesized in HCl, HNO_3 and $HClO_4$ were rutile phase with rhombus shape, while anatase TiO_2 with flake shape was gained in H_2SO_4 system. Kutty et al. [12] synthesized fine powders of TiO_2 with high degree of crystallinity from $TiOCl_2$ solution by hydrothermal method. They found that SO_4^{2-} anions could retard the formation of rutile. Later, in Cheng et al.'s work [13], rodlike nanoparticles of rutile were prepared by using $TiCl_4$ as the titanium source, and the formation of rutile was ascribed to a growth unit with negative charge and consisting of Cl^- anions. The study of Agatino et al. [14] indicated that the relative proportions of the TiO_2 polymorphic phases obtained by thermolysis of $TiCl_4$ in HCl solutions were mainly depend on the total concentration of HCl in the precipitation solution. So, it is reasonable to conclude that the nature and concentration of acid played an important role in synthesis of TiO_2. However, the preparation of TiO_2 photocatalyst by chemical reagents containing Ti is not suitable for real industry application due to its high cost. Therefore, how to synthesize TiO_2 photocatalysts with different crystalline phases from low cost raw natural materials, especially solid wastes by using effective method is still a challenge issue.

Ti-bearing slags such as Ti-bearing blast furnace slag (Ti-bearing BF slag) and Ti-bearing electric arc furnace molten slag (Ti-bearing EAF slag) etc., are considered as valuable secondary resources in China due to their relatively higher Ti contents. Considering the cost of the solid wastes, Li et al.[15, 16] proposed a novel process which includes molten NaOH treatment, hydrolysis, acidolysis and calcination, to prepare nanostructured TiO_2 photocatalyst from Ti-bearing EAF slag. According to above analysis, it is known that the textural properties of obtained TiO_2 from chemical reagents determined as a function of the nature and concentration of the inorganic acid used for the synthesis. So, the effect of acidic medium used in the acidolysis process on the prepared TiO_2 should not be neglected in the novel system. However, the influence of acid species and concentration on crystalline phase and morphology of TiO_2 synthesized from Ti-bearing EAF slag was seldom investigated, especially the transformation mechanism of TiO_2 in different inorganic acids with different concentrations were not clear.

In this paper, nanostructured TiO_2 were synthesized from Ti-bearing EAF slag. The effects of acid species and concentrations on the crystalline phases and morphologies of TiO_2 were systemically investigated. And the TiO_2 crystal phase transformation mechanism and morphology evolution in different acid systems during the acidolysis process and concentrations were discussed in detail. In addition, the photocatalytic properties of as-prepared TiO_2 in different acid systems were also examined.

2. Experimental

2.1 Materials

The Ti-bearing EAF slag samples were provided by Panzhihua Steel Company (Sichuan Province, China), which were obtained from vanadium-titanium magnetite concentrate through direct reduction reaction by rotary hearth furnace and smelting separation by electric furnace. The slag's main chemical compositions and phase structure were shown in Table 1 and Fig. 1, respectively. As shown in Fig. 1, it is indicated that the Ti-bearing phases of the slag were anosovite solid solution ($M_xTi_yO_5$, x+y=3, M=Mg, Fe, Ti) and Mg_2TiO_4, while the main impurity phases were $MgAl_2O_4$ and amorphous metasilicate.

All the chemical regents employed were analytical grade (Sinopharm Chemical Reagent Co. Ltd) and the distilled water was used throughout the experiment.

Insert Fig. 1

Table 1 Main chemical compositions of the Ti-bearing EAF slag wt.%

Composition	TiO_2	Al_2O_3	MgO	SiO_2	CaO	Fe_2O_3
Content	50.9	19.4	12.9	8.0	5.4	2.9

2.2 Sample characterization

Chemical compositions were analyzed by inductively coupled plasma optical emission spectroscopy (ICP-OES, TELEDYNE Leeman Labs). The phase structure was investigated by X-ray diffraction using Cu Kα radiation (λ=0.154056 nm) with 40 kV, 200 mA and a speed of 10° min^{-1} (XRD, M21X, MAC SCIENCE Co. Ltd, Japan). The morphology and microstructure of the samples were examined by field emission scanning electron microscopy (SEM, Zeiss, Supra-55) and transmission electron microscopy (TEM, FEI, F20), the amount of ionic doping in products was analyzed by

energy-dispersive X-ray spectroscopy attached with SEM (EDS, Zeiss, Supra-55). X-ray photoelectron spectroscopy (XPS, AXIS Ultra) was used to analyze the atomic surface state on each sample with Al K α X-rays. The BET surface area was determined by the N_2 adsorption/desorption isotherms (Micrometrics, ASAP 2010). The absorption spectra of the samples were tested by a UV-Vis spectrophotometer (Persee , TU-1901).

2.3 Experimental process

2.3.1 Synthesis of nanostructured TiO_2 and separation principle

The general flow sheet of the process for synthesis of nanostructured TiO_2 from Ti-bearing EAF slag was illustrated as Fig. 2. In detail, the Ti-bearing EAF slag was ground to about 120 mesh and mixed with NaOH homogeneously with Ti-bearing EAF slag/ NaOH mass ratio ($R_{slag/NaOH}$) at 1:1.5 in the nickel crucible. Then, the nickel crucible was placed into a muffle furnace and heated to 700°C, holding for 1 h with free access to air. After the molten NaOH treatment process, the nickel crucible was taken out rapidly and then cooled at room temperature. The obtained slag was called alkali fusion slag. According to our previous research, it is known that the main composition of the alkali fusion slag were Na_2TiO_3, $NaMO_2$ (M=Ti, Mg and Fe), $NaAlO_2$ and amorphous sodium silicate, and the corresponding reactions of Ti-bearing EAF slag with the molten NaOH can be described as follows:

$$M_xTi_yO_5+4NaOH \longrightarrow Na_2TiO_3+2NaMO_2+2H_2O \quad (x+y=3,\ M=Ti,\ Mg,\ Fe) \qquad (1)$$

$$MgAl_2O_4+2NaOH \longrightarrow 2NaAlO_2+MgO+H_2O \qquad (2)$$

$$MgSiO_3+CaSiO_3+4NaOH \longrightarrow 2Na_2SiO_3+CaO+MgO+2H_2O \qquad (3)$$

Then the alkali fusion slag was ground to about 200 meshes and 3 g ground alkali fusion slag was leached in 300 ml distilled water with magnetic stirring for 1 h. After that, the slurry was filtered and the residue was dried in oven at 80°C for 24 h. During this process, the water soluble sodium salts such as Na_2SiO_3 and $NaAlO_2$ could be separated from the water insoluble sodium titanate salts based on their different solubility in water. In the meantime, most of Na_2TiO_3 would be converted to $Na_{2-x}H_xTiO_3$ according to the following equation (4) [17] and the rest still existed as Na_2TiO_3:

$$Na_2TiO_3+2H_2O \longrightarrow Na_{2-x}H_xTiO_3+2NaOH \qquad (4)$$

As for the acidolysis process, 200 ml different acid solutions with different concentrations were mixed with the residue obtained from water leaching in flask and then heated to boiling by heating jacket with standard reflux apparatus for 6 h. After filtration, hydrated TiO_2 was obtained, and the related reactions during this procedure can be illustrated as follows:

$$Na_2TiO_3+4H^+ \longrightarrow Ti(OH)_2^{2+}+2Na^++H_2O \qquad (5)$$

$$Na_{2-x}H_xTiO_3+(4-x)H^+ \longrightarrow Ti(OH)_2^{2+}+(2-x)Na^++H_2O \qquad (6)$$

$$Ti(OH)_2^{2+}+H_2O \xrightleftharpoons{\text{boiling}} H_2TiO_3+2H^+ \qquad (7)$$

Insert Fig. 2

Finally, the obtained residue was dried in oven at 80°C for 24 h and calcined in muffle furnace at 500°C for 1 h to prepare nanostructured TiO_2. It should be noted that the acidolysis process was the key step to determine the type of crystalline phase and morphology of obtained nanostructured TiO_2 from Ti-bearing EAF slag. Therefore, this paper was mainly focus on the acidolysis process of sodium titanate with different types of acids at different concentrations in order to elucidate the transformation mechanism of nanostructured TiO_2 clearly.

2.3.2 Photocatalytic activity measurements

The photocatalytic activity of obtained nanostructured TiO_2 from Ti-bearing EAF slag with different acids was investigated by measuring the photodegradation efficiency of rhodamine B aqueous solution. Photocatalytic reactions under the visible light irradiation were carried out in a quartz glass reactor equipped with a magnetic stirrer and a collimated light source. 0.05g as-prepared TiO_2 and 200 mL rhodamine B aqueous solution (5 $mg\cdot L^{-1}$) were placed into the reaction vessel. O_2 was continuously bubbled into the solution for 20 min before switching on the lamp and throughout the occurrence of the photocatalytic reactions. At the given intervals of parallel light irradiation, the samples of 5 ml were withdrawn from the solution and the catalyst was separated from the solution by filtration. The quantitative determination of rhodamine B solution was performed by measuring its absorption with a UV-Vis spectrophotometer. In addition, the control experiments without photocatalysts and without light irradiation were also conducted (ESI, 2).

The photodegradation efficiency (η) was evaluated as the follows:

$$\eta=100\%\times\left(\frac{A_0-A_t}{A_0}\right) \qquad (8)$$

where A_0 and A_t ($mg\cdot L^{-1}$) are the concentrations of rhodamine B solution at the beginning and after illumination for t (min) time, respectively.

3. Results and discussion

During the acidolysis process, the reactions occurred between the residue ($Na_2TiO_3/Na_{2-x}H_xTiO_3$) and acid solution can be regarded as liquid-solid reactions (eqs. (5-7)). The residue obtained from water leaching process might be dissolved in acid solution and then Ti ions would form TiO_2 crystal nucleus on the surface of undissolved residue by heterogeneous nucleation, and in the meantime, ion exchange reaction would also occur between the rest undissolved residue and H^+ to form hydrated TiO_2, which can be converted to TiO_2 by drying and calcination. The two competitive reactions, namely, dissolution reaction and H^+ ion exchange reaction would happen simultaneously. According to the distribution of titanium species at different pH values (Fig. 3 [18]), it is shown that Ti element has three existence forms including $Ti(OH)_2^{2+}$, $Ti(OH)_3^+$ and $Ti(OH)_4$ when the solution pH value is below 7. Since the acidolysis process was conducted at pH value below 1, the Ti element would mainly exist as $Ti(OH)_2^{2+}$ ions in the solution, which means that the dissolution reaction (eqs. (5-7)) between $Na_2TiO_3/Na_{2-x}H_xTiO_3$ and acid solution would be the key reaction during the acidolysis process.

Insert Fig. 3

Considering the anions existed in acid solution, the $Ti(OH)_2^{2+}$ would combine with H_2O or anion such as Cl^-, NO_3^- or HSO_4^{2-} to form a complex six-fold coordinated monomer with octahedral coordinated structure, which has the formula $[Ti(OH)_2R_n(OH_2)_m]^{2-n}$, where n+m=4 and R=$Cl^-$, NO_3^- or HSO_4^-

. Then, the presence of aquo and hydroxo ligands in the coordination sphere of this complex allows the condensation by olation, which involves the elimination of aquo ligands and formation of dimers and small chains. These dimmers or small chains would link together by further condensation to process oxolation reaction with HR elimination and formation oxo bridges between octahedrons, resulting in the precipitation of polymers with cross-linked networks. The polymers gave rise to, by dehydration, TiO_2 with different crystalline phases. In addition, since the anions existed in acid solution have different spatial radius and steric hindrance effect, they could play a role of template to help the formation of TiO_2 crystal with different morphologies. So, the acidolysis process was the key step to determine the type of crystalline phase and morphology of the final products.

3.1 Effect of acid species during the acidolysis process

In this part, different inorganic acids such as HCl, H_2SO_4 and HNO_3 were used to investigate the effect of acids species on the crystalline phase of the obtained nanostructured TiO_2. For the sake of identical H^+ concentration, HCl, HNO_3, H_2SO_4 solutions with respective concentrations of 0.9, 0.9, and 0.45 $mol{\cdot}L^{-1}$ were used to examine the function of different anions. Fig. 4 gave the XRD patterns of samples obtained from different acids. It can be seen that the all products were TiO_2 with different crystalline phases. Specifically, anatase type TiO_2 was mainly obtained from H_2SO_4 solution while rutile type TiO_2 was gained from HCl solution. Both of the two types including anatase and rutile TiO_2 was achieved from HNO_3 solution and the amount of anatase was more than that of rutile.

Insert Fig. 4

Generally, rutile, anatase and brookite are three polymorphs of TiO_2 existed in nature. However, the fundamental structure units in these crystals are all $[TiO_6]$ octahedrons, only their modes of arrangement and link are different. In rutile, $[TiO_6]$ octahedrons link by sharing an edge along the c axis to form chains and then corner-shared bonding among chains leads to a three-dimensional framework. In anatase, the formation of a three-dimensional framework is all with edge-shared bonding among $[TiO_6]$ octahedrons. The structure of brookite is slightly complicated and contains either edge-shared bonding or corner-shared bonding [19].

Insert Fig. 5

Bearing the structures of the titania polymorphs in mind, it is obvious that linear chains can only form rutile type nuclei, while skewed chains can only form anatase type nuclei [20]. The mechanism of the formation of anatase and rutile from $[TiO_6]$ octahedrons can be illustrated by Fig. 5. It was reasonable to assume that R in $[Ti(OH)_2R_n(OH_2)_m]^{2-n}$ occupied *a* position while OH and H_2O occupied *b* position to illustrate the polymerization process between $[Ti(OH)_2R_n(OH_2)_m]^{2-n}$ monomers. Since the ion radius sorting was $HSO_4^- > OH^- > NO_3^- > Cl^-$, the Cl^- would be eliminated after all the water molecular were removed (the chloride ions being more strongly bound groups than hydroxy ligands). In that case, when the concentrate of H^+ and amount of Cl^- were identical in HCl system, $Ti(OH)_2Cl_2(OH_2)_2$ octahedrons would prior to link together by sharing equatorial edges with aquo ligands elimination to form linear chains. Then, a three-dimensional network was formed by sharing vertices with HCl elimination, resulting in the formation of rutile type TiO_2 [19, 21] as indicated in Fig. 5a. However, the ion radius of HSO_4^- was larger than that of OH^-, so, HSO_4^- in $Ti(OH)_2(HSO_4)_2(OH_2)_2$ monomers would be eliminated with aquo ligands elimination and formation of skewed chains [22]. Then the skewed chains polymerized further by oxolation led to the formation of the anatase type TiO_2 as shown in Fig. 5b. Because the ion radius of NO_3^- was between that of HSO_4^- and Cl^-, it means both of the linear chains or skewed chains might be formed in HNO_3 system. As a result, the sample obtained from HNO_3 system consisted of rutile and anatase TiO_2.

Fig. 6 gave the SEM images of samples synthesized in different acid systems. It can be seen that the sample obtained in H_2SO_4 was spherical particles with many protuberances on their surfaces (Fig. 6a). The samples synthesized in HCl or HNO_3 system was nearly all needle-like nanorod clusters (Fig. 6b and 6c).

Insert Fig. 6

Fig. 7 illustrated TEM images of samples obtained in different acid systems. It is shown that each spherical particle obtained in H_2SO_4 was composed of many nanoparticles with average size of 5 nm (inset in Fig. 7a). The lattice spacing (0.35±0.005 nm) of each nanoparticle shown in Fig. 7a was assigned to the (101) planes in anatase type TiO_2, indicating the nanoparticle was single crystalline structure of anatase. In addition, the samples synthesized in HCl or HNO_3 systems both had needle-like structures with average length of 50 nm (shown as insets in Fig. 7b and 7c). From the HRTEM images (insets in Fig. 7b and 7c), it can be seen that the lattice spacing were about 0.32±0.005, which belonged to the (110) planes in rutile type TiO_2, further confirming that the as-prepared nanorod structures were rutile type TiO_2.

Insert Fig. 7

The products with different morphologies were determined by the structure of the polymorphs and their organization during the crystal nucleus growth process. Since HSO_4^{2-} or SO_4^{2-} has huger spatial radius and larger steric hindrance effect compared with NO_3^- and Cl^- ions, which can adsorb on every crystal face resulting in the crystal growth without orientation [10]. So, the samples obtained in H_2SO_4 system existed as spherical clusters. However, the ion radius of NO_3^- and Cl^- were smaller and the charge number of them were less compared to SO_4^{2-}, indicating that NO_3^- and Cl^- prefer to adsorb on the (110) and (101) planes, leading to these ions have stronger ability to restrain the radial growth of the crystals [16, 23]. As a result, the samples obtained in HCl or HNO_3 systems had needle like structures.

3.2 Effect of H_2SO_4 concentration during the acidolysis process

Fig. 8 gave the XRD patterns of samples prepared in H_2SO_4 system with different H_2SO_4 concentrations. It can be seen that only the diffraction peaks of anatase type TiO_2 appeared when the acid concentration was 0.3 $mol{\cdot}L^{-1}$, suggesting that the sample obtained in H_2SO_4 solution with concentration fixed at 0.3 $mol{\cdot}L^{-1}$ was single phase of anatase type TiO_2. With the increasing of H_2SO_4 concentration to 0.6 $mol{\cdot}L^{-1}$, a weak diffraction peak indexed to rutile type TiO_2 appeared at $2\theta = 25.38°$, indicating that mixtures of anatase and rutile type of TiO_2 with a higher fraction of anatase were

obtained. Further increasing H_2SO_4 concentration to 0.75 and 1 mol·L^{-1}, the diffraction peak intensity of rutile type TiO_2 at 2θ = 25.38° became strong, suggesting that the amount of rutile type TiO_2 was increased with the H_2SO_4 concentration increasing.

Insert Fig. 8

Depending on the analysis of the XRD patterns, it is known that the product obtained in H_2SO_4 system would change from anatase to rutile type TiO_2 spontaneously with the increasing of H_2SO_4 concentration. On the basis of the crystal nucleus formation mechanism shown in Fig. 5, a possible transformation mechanism of anatase changed to rutile type TiO_2 was proposed, which could be illustrated as Fig. 9.

Insert Fig. 9

According to the reference [22], titanium would combine with SO_4^{2-} or HSO_4^- to form $Ti(OH)_2SO_4(H_2O)_3$ or $Ti(OH)_2(HSO_4)_2(H_2O)_2$ complex ions in H_2SO_4 system. In their opinion, this structure prefer to link together to form an infinite zigzag of –Ti–O–Ti–O– chains (Fig. 9a). Titanium is octahedrally coordinated by two bridging oxygen atoms, an oxygen atom from each of three sulphate ions, and one water molecule. Based on the aforementioned analysis, the zigzag of –Ti–O–Ti–O– chains were skewed chains, which was prior to form the anatase type TiO_2 by edge-shared polymerization (Fig. 9b). However, when the H_2SO_4 concentration increased, the formed zigzag chains of $[TiO_6]$ octahedrons might be resolved into detached $[TiO_6]$ octahedron or their small clusters (Fig. 9c). These detached $[TiO_6]$ octahedrons or small clusters might link to each other by sharing vertices during the restacking process, resulting in three-dimensional lattices with corner-shared bonding (Fig. 9d). Thus, rutile type TiO_2 appeared in concentrated H_2SO_4 system. So, TiO_2 nanostructures obtained in H_2SO_4 system would be apt to change from anatase to rutile with the increasing of H_2SO_4 concentration.

Insert Fig. 10

Fig. 10 is SEM images of samples obtained in H_2SO_4 system with different acid concentrations. It can be seen that the sample existed as granular mosaic structure when the acid concentration was 0.3 mol·L^{-1} (Fig. 10a). With the acid concentration increasing to 0.6 and further to 1.0 mol·L^{-1}, the morphologies of the obtained samples changed to spherical clusters with many protuberances on their surfaces (Fig. 10a, b, c). Associated with the XRD patterns shown in Fig. 8, it was reasonable to assume that the protuberances on the surfaces of spherical clusters were the morphologies of rutile type TiO_2, which transformed from anatase to rutile type TiO_2 with increasing H_2SO_4 concentration. The rutile has anisotropic characteristic and prefers to grow along c axis, forming nanorod structures [20, 24], which would result in protuberances on the surfaces of already formed spherical clusters. Fig. 11 illustrated TEM images of samples obtained in H_2SO_4 system with acid concentration at 0.3 and 1.0 mol·L^{-1}, respectively. As shown in Fig. 11a, the prepared sample was composed of spherical nanoparticles when the H_2SO_4 solution concentration was 0.3 mol·L^{-1}. The lattice spacing (0.35±0.005 nm) of each nanoparticle shown in the HRTEM image (insets in Fig. 11a) was assigned to the (101) planes in anatase type TiO_2, indicating the nanoparticle was single crystalline structure of anatase. However, when the H_2SO_4 solution concentration increased to 1.0 mol·L^{-1}, there were some nanorod structure appeared on the surfaces of obtained spherical nanoparticle clusters. From the HRTEM image (insets in Fig. 11b), it can be seen that the lattice spacing were about 0.32±0.005, which belonged to the (110) planes in rutile type TiO_2, further confirming that the as-prepared nanorod structures were rutile type TiO_2.

Based on the aforementioned analysis, it is reasonable to conclude that both the acid species and concentration played important roles in the formation of different TiO_2.

Insert Fig. 11

3.3 Photocatalytic properties of samples obtained from different acid systems

Fig. 12a gives the UV-vis absorption spectra of samples obtained from different acid systems. The absorption spectra of the samples had some degree of red shift. And the corresponding absorption edges of samples obtained in H_2SO_4, HCl and HNO_3 system were 396, 430 and 404 nm, respectively. Their band gap energies can be calculated by the following equation:

$$\alpha h\nu = A(h\nu - Eg)^n \quad (9)$$

where h is the Planck's constant, ν is the frequency of light, A is a constant, and n is equal to 2 for an allowed indirect transition or 1/2 for an allowed direct transition [25]. As for TiO_2, the transition is direct and therefore $(\alpha h\nu)^2$ is plotted as a function of hν from which the band gap energy could be attained by Tauc Plot. The band gap energies estimated by extrapolating a straight line to the abscissa axis from the plots and the results were shown in Fig. 12b. The band gap energies of TiO_2 (3.06, 3.02 and 2.95 eV) were all nearly narrower than that of pure TiO_2 (3.20 eV), which might be ascribed to the doping of different ions in the solution. From the EDS analysis results in Table 2, it can be seen that Fe and Si were doped into the samples with different weight percentages, leading to the band gap energies of TiO_2 decreasing.

Insert Fig. 12

Table 2 EDS analysis of samples synthesized from Ti-bearing EAF slag in different acid systems

Element	Weight %		
	HCl	HNO_3	H_2SO_4
C K	26.54	23.70	23.91
O K	34.91	40.32	36.17
Ti K	35.12	32.47	38.01
Si K	0.50	0.67	-
Fe K	2.92	2.84	1.90
Total	100.00	100.00	100.00

In order to confirm the doping of these of elements, XPS spectroscopy was utilized to detect elements and determine their chemical states in prepared samples. From the wide survery spectra of the samples synthesized from different acids, titanium and oxygen peaks were identified obviously, and the carbon peak was attributed to the adventitious hydrocarbon as shown in Fig. S1. Fig. 13 showed the Ti 2p, O1s, Fe 2p and Si 2p high resolution spectra of the as-prepared TiO_2. It should be noted from Fig. 13(c-d) that Fe and Si elements co-exist in the

TiO_2 samples and the valence states were +3 (Fe) and +4 (Si), respectively. The binding energies of the double peaks were around 458.3 eV and 464.1 eV for Ti $2p_{3/2}$ and Ti $2p_{1/2}$. The energy position of this doublet only corresponded to the Ti^{4+} oxidation state, suggesting that none of Ti^{3+} existed in all the products.

In addition, it can be clearly seen from Fig. 13(a) that the binding energy of Ti $2p_{2/3}$ peak for as-prepared TiO_2 was 458.5-458.8 eV, which was 0.2-0.5 eV greater than that of pure TiO_2. The decrease of the electron density around Ti atom might be due to the greater electronegativity of Si via O acting on Ti [26]. The shielding effect was weakened, and then the binding energy was increased. This result proved the formation of Ti–O–Si bond in the as-prepared TiO_2. In addition, the substitution of Fe^{3+} for tetravalent Ti^{4+} in TiO_2 and formation of Ti-O-Fe bond would create oxygen deficiency, also leading to the gradual peak shift of Ti 2p.

As the O1s spectra shown in Fig. 13(b), the pure TiO_2 of O1s was located at 529.5 eV, corresponding to lattice oxygen of TiO_2. The shift of O1s spectra from 529.5 eV (for pure TiO_2) to 529.8–530.1 eV (for as-prepared TiO_2) suggested that Fe^{3+} or Si^{4+} ions were doped into TiO_2.

Based on the aforementioned analysis, it is reasonable to assume that Fe^{3+} and Si^{4+} ions were co-doped into TiO_2.

Insert Fig. 13

Fig. 14 gives the absorption spectra of rhodamine B solutions in the presence of TiO_2 obtained in different acid systems. It is shown that all the absorbances of rhodamine B solutions decreased obviously with prolonging the illumination time, suggesting that rhodamine B solutions can be photodegraded by the TiO_2 samples under the visible light illumination. Moreover, the maximum absorption wavelengths of the degraded solutions exhibited hypsochromic shifts to a certain degree, which might be ascribed to the stepwise formation of a series of N-deethylated intermediates [27].

Insert Fig. 14

According to the formular (8), the corresponding photodegradation efficiencies of TiO_2 photocatalysts obtained in different acid systems were shown in Fig. 15. The relatively higher photodegradation efficiency of the TiO_2 obtained from H_2SO_4 system can reach 90.52%, while that of the other two samples synthesized from HNO_3 and HCl were 85.22% and 79.65%, respectively. This case might be attributed to the different crystal phases and specific surface areas of as-prepared TiO_2. The larger specific surface area may generate more active sites for adsorbing oxygen atoms to form active hydroxyl groups, which leads to the photocatalytic activity improved [28]. As shown in Fig. 6 and 7, the TiO_2 obtained from H_2SO_4 was spherical particle composed of many nanoparticles with average size of 5 nm, resulting in larger specific surface area of 162 $m \cdot g^{-1}$. Whereas, the samples synthesized in HCl and HNO_3 both were needle-like nanorod clusters with average length of 50 nm, leading to decreased specific surface area of 152 and 150 $m \cdot g^{-1}$, respectively. Moreover, the band gap energy of the sample obtained from H_2SO_4 was the largest (3.06 eV), implying it had higher redox potential than that of the others, which could also increase the photodegradation efficiency correspondingly.

In addition, the control experiments without photocatalysts and without light irradiation were carried out to confirm the photocatalysis property of as prepared TiO_2 and the results were shown in Fig. S2. It can be seen from Fig. S2a that the adsorption-desorption equilibrium between catalyst and rhodamine B can be reached in only 15 min and the adsorption rate was about 11.8%. As shown in Fig. S2b, the photodegradation efficiency of rhodamine B under visible light irradiation without catalyst was only about 13% in 90 min. Therefore, the as-prepared TiO2 photocatalysts played key role in degradation of rhodamine B.

Insert Fig. 15

4. Conclusions

Nanostructured TiO_2 photocatalysts with different crystalline phases and morphologies were synthesized from Ti-bearing EAF slag. The influences of acid species and H_2SO_4 concentrations during the acidolysis process on the crystal phases and morphologies of TiO_2 were studied. And the TiO_2 crystal phase transformation mechanism and morphology evolution in different acid species and concentrations were discussed in detail. It is shown that rutile type TiO_2 with needle-like nanorod structures and anatase type TiO_2 with spherical nanoparticle structures were preferred to be obtained from HCl and H_2SO_4, respectively, while two types coexisted with needle-like nanorod structures in HNO_3. Moreover, anatase type TiO_2 would be apt to change to rutile type TiO_2 with increasing of H_2SO_4 concentration. Moreover, the photocatalytic properties of nanostructured TiO_2 photocatalysts were evaluated by photodegradation of rhodamine B solutions. The nanostructured TiO_2 synthesized from H_2SO_4 showed better photocatalytic activity than that from HCl or HNO_3, and its photodegradation efficiency can reach 90.52% in 90 min for rhodamine B solution.

Acknowledgements

This study was supported by the National Basic Research Program of China (No. 2014CB643401, 2013AA032003), the National Nature Science Foundation of China (NOs. 51372019, 51277025 and 51072022).

References

1. Y. Wang, J. Li, L. Wang, T. Xue and T. Qi, *Ind. Eng. Chem. Res.*, 2010, **49**, 7693-7696.
2. N. Serpone and A. V. Emeline, *J. Phys. Chem. Lett.*, 2012, **3**, 673-677.
3. A. Fujishima and X. Zhang, *C. R. Chim.*, 2006, **9**, 750-760.
4. F. Ren, X. Yu, Y. Ling and J. Feng, *Int. J. Min. Met. Mater.*, 2012, **19**, 461-466.
5. J. Shi, C. Sun, M. B. Starr and X. Wang, *Nano Lett*, 2011, **11**, 624-631.
6. L. Dong, K. Cheng, W. Weng, C. Song, P. Du, G.

Shen and G. Han, *Thin Solid Films*, 2011, **519**, 4634 - 4640.
7. N. Sasirekha, B. Rajesh and Y. Chen, *Thin Solid Films*, 2009, **518**, 43-48.
8. Q. X. Deng, M. D. Wei, Z. S. Hong, X. K. Ding, L. L. Jiang and K. M. Wei, *Curr. Nanosci.*, 2010, **6**, 479-482.
9. K. Sabyrov, N. D. Burrows and R. L. Penn, *Chem. Mater.*, 2013, **25**, 1408-1415.
10. M. Wu, G. Lin, D. Chen, G. Wang, D. He, S. Feng and R. Xu, *Chem. Mater.*, 2002, **14**, 1974-1980.
11. B. Rajesh, N. R. Sasirekha and Y. W. Chen, *Mater. Res. Bull.*, 2008, **43**, 682-692.
12. T. R. N. Kutty, R. Vivekanandan and P. Murugaraj, *Mater. Chem. Phys.*, 1988, **19**, 533-546.
13. H. Cheng, J. Ma, Z. Zhao and L. Qi, *Chem. Mater.*, 1995, **7**, 663-671.
14. A. Di Paola, G. Cufalo, M. Addamo, M. Bellardita, R. Campostrini, M. Ischia, R. Ceccato and L. Palmisano, *Colloids and Surfaces A*, 2008, **317**, 366-376.
15. Y. Li, Y. Yue, Z. Que, M. Zhang and M. Guo, *Inter. J. Min. Met. Mater.*, 2013, **20**, 1012-1020.
16. Z. Que, Y. Li, H. Yu, F. Zheng, M. Zhang and M. Guo, *Rare Metals*, 2013, **9**, 1-9.
17. Y. H. Liu, W. Zhao, W. J. Wang, X. Yang, J. L. Chu, T. Y. Xue, T. Qi, J. Y. Wu and C. R. Wang, *J. Phys. Chem. Solids*, 2012, **73**, 402-406.
18. Y. Fovet, J. Gal and F. Toumelin-Chemla, *Talanta*, 2001, **53**, 1053-1063.
19. H. Cheng, J. Ma, Z. Zhao and L. Qi, *Chem. Mater.*, 1995, **7**, 663-671.
20. L. Shen, N. Bao, Y. Zheng, A. Gupta, T. An and K. Yanagisawa, *J. Phys. Chem. C*, 2008, **112**, 8809-8818.
21. J. H. Lee and Y. S. Yang, *J. Eur. Ceram. Soc.*, 2005, **25**, 3573-3578.
22. K. C. Sole, *Hydrometallurgy*, 1999, **51**, 239-253.
23. Y. Li, M. Guo, M. Zhang and X. Wang, *Mater. Res. Bull.*, 2009, **44**, 1232-1237.
24. W. Li, E. Shi and Z. Yin, *J. Cryst. Growth*, 2000, **208**, 546-554.
25. J. Su, X. Feng, J. D. Sloppy, L. Guo and C. A. Grimes, *Nano Lett.*, 2010, **11**, 203-208.
26. R. Jin, Z. Wu, Y. Liu, B. Jiang and H. Wang, *J. Hazard. Mater.,* 2009, **161**, 42–48.
27. C. Chen, W. Zhao, P. Lei, J. Zhao and N. Serpone, *Chem.- Eur. J.*, 2004, **10**, 1956-1965.
28. X. Chen and S. S. Mao, *Chem. Rev.*, 2007, **107**, 2891-2959.

Figure captions:

Fig. 1 XRD pattern of the Ti-bearing EAF slag

Fig. 2 Flow sheet of the process for synthesis of nanostructured TiO_2 from Ti-bearing EAF slag

Fig. 3 The distribution of titanium species without anions in solutions with different pH values (reprinted with permission from ref. 18; Copyright @ 2001 Elsevier)

Fig. 4 XRD patterns of TiO_2 synthesized from Ti-bearing EAF slag in different acid systems

Fig. 5 The formation mechanism of anatase and rutile from octahedron formed in different acids systems

Fig. 6 SEM images of TiO_2 synthesized from Ti-bearing EAF slag in different acid systems (a) H_2SO_4; (b) HCl; (c) HNO_3

Fig. 7 TEM and HRTEM images (insets) of TiO_2 synthesized from Ti-bearing EAF slag in different acid systems (a) H_2SO_4; (b) HCl; (c) HNO_3

Fig. 8 XRD patterns of TiO_2 synthesized from Ti-bearing EAF slag with different H_2SO_4 concentrations

Fig. 9 The mechanism of phase transformation from $Ti(OH)_2(HSO_4)_2$ to anatase and rutile in different acid concentration solutions

Fig. 10 SEM images of samples obtained in sulfuric acid system with different acid concentrations (a) 0.3 $mol\cdot L^{-1}$; (b) 0.6 $mol\cdot L^{-1}$; (c) 0.9 $mol\cdot L^{-1}$; (d) 1.0 $mol\cdot L^{-1}$

Fig. 11 TEM and HRTEM images (insets) of TiO_2 synthesized from Ti-bearing EAF slag in sulfuric acid system with different acid concentrations (a) 0.3 $mol\cdot L^{-1}$; (b) 1.0 $mol\cdot L^{-1}$

Fig. 12 (a) UV-vis absorption spectra of TiO_2 obtained from Ti-bearing EAF slag in different acid systems; (b) $(ah\nu)^2$ is ploted as a function of $h\nu$ from which the band gap energy is obtained by Tauc Plot

Fig. 13 Ti 2p and O 1s XPS spectra of pure TiO_2 and as-synthesized TiO_2 from different acid systems (a) Ti 2p; (b) O 1s

Fig. 14 Absorbance spectra of rhodamine B solutions in the presence of TiO_2 obtained in different acid systems (a) H_2SO_4; (b) HNO_3; (c) HCl

Fig. 15 The photodegradation efficiencies of nanostructured TiO_2 obtained from different acid solutions

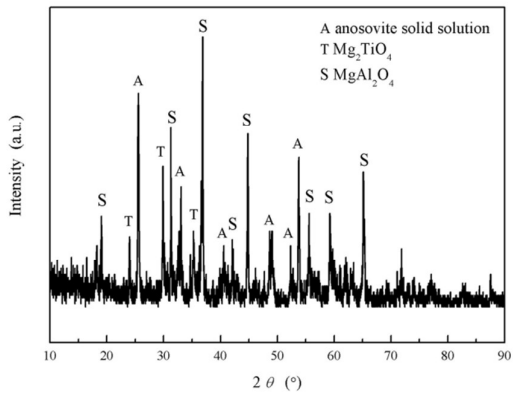

Fig. 1

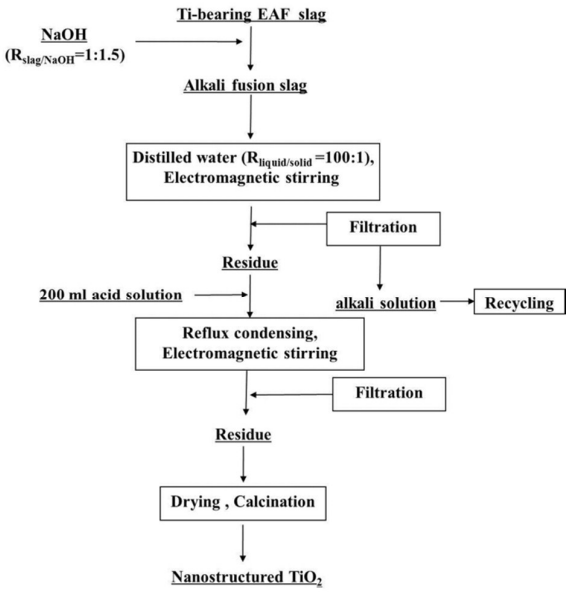

Fig. 2

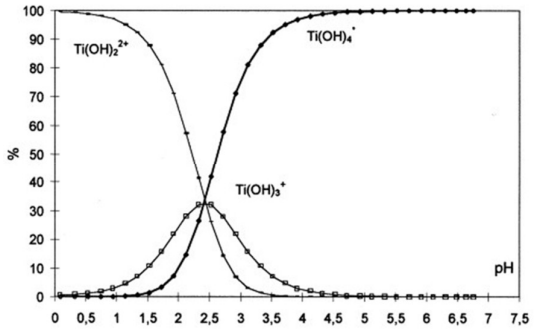

Fig. 3

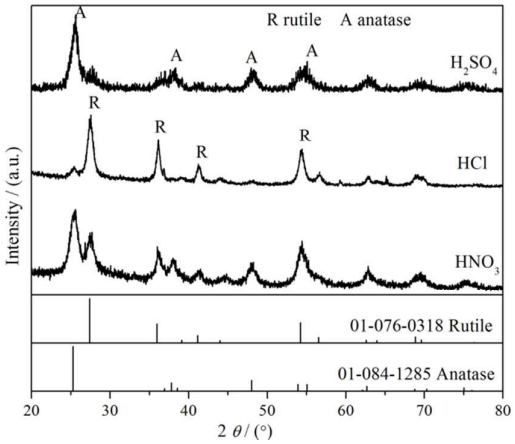

Fig. 4

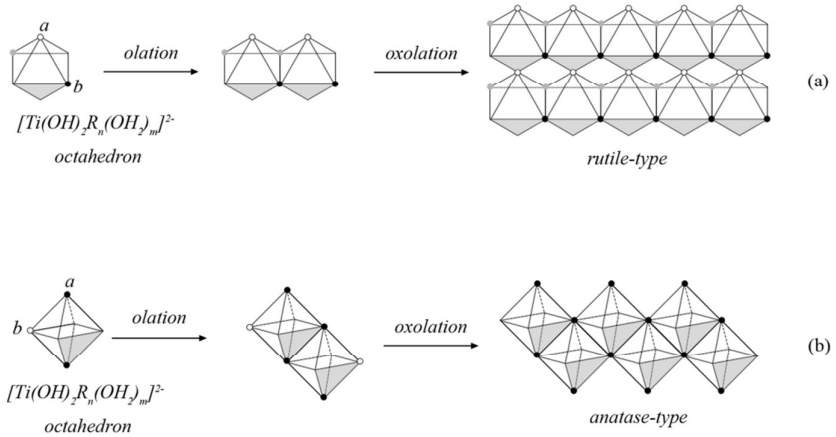

Fig. 5

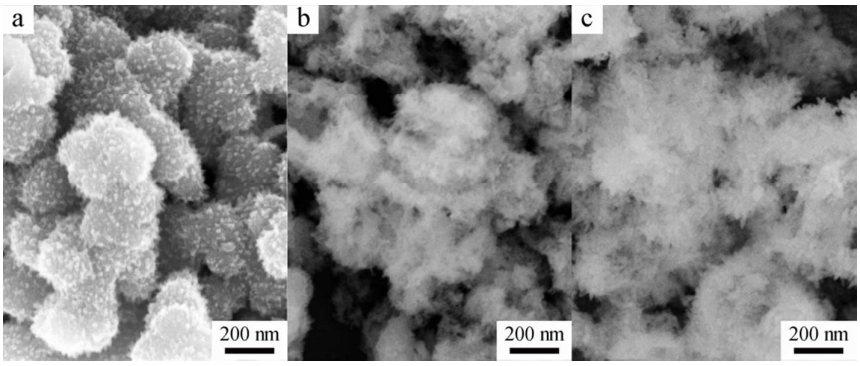

Fig. 6

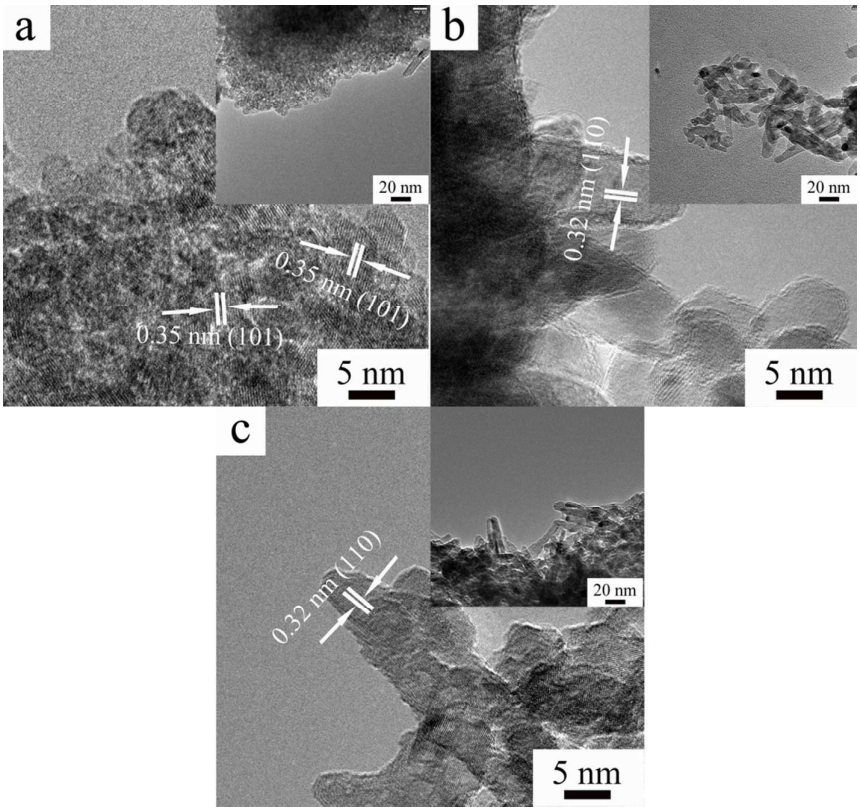

Fig. 7

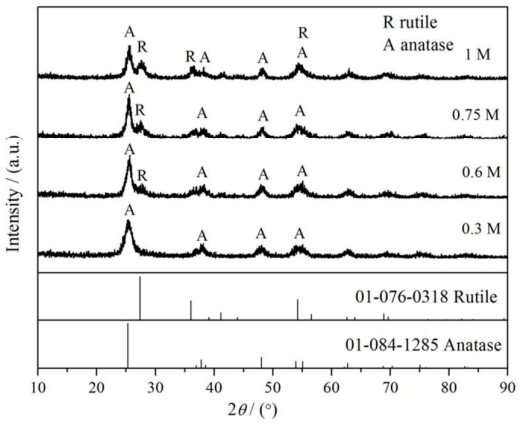

Fig. 8

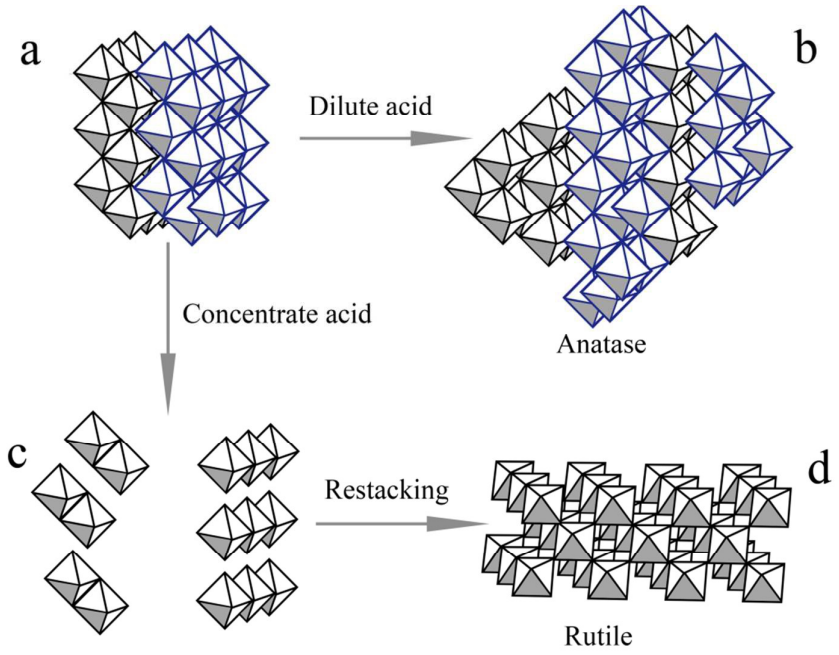

Fig. 9

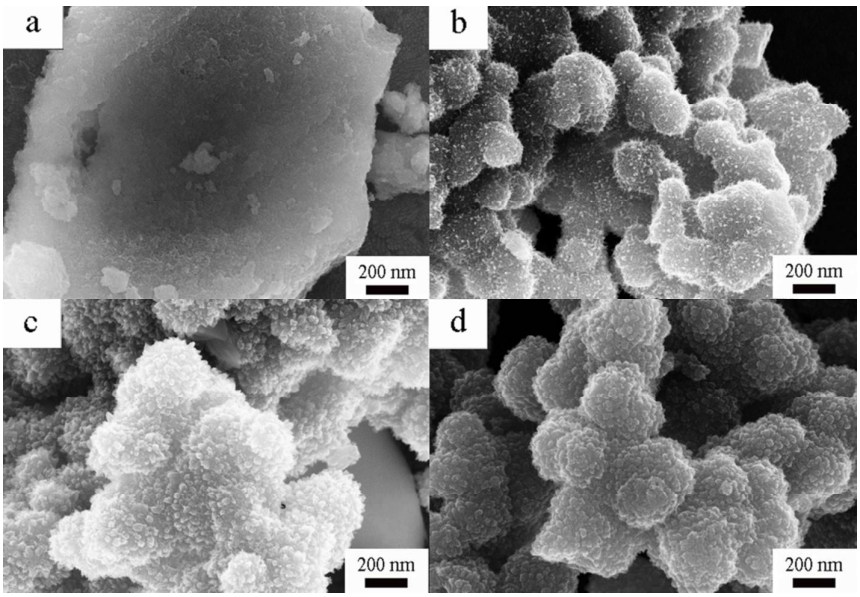

Fig. 10

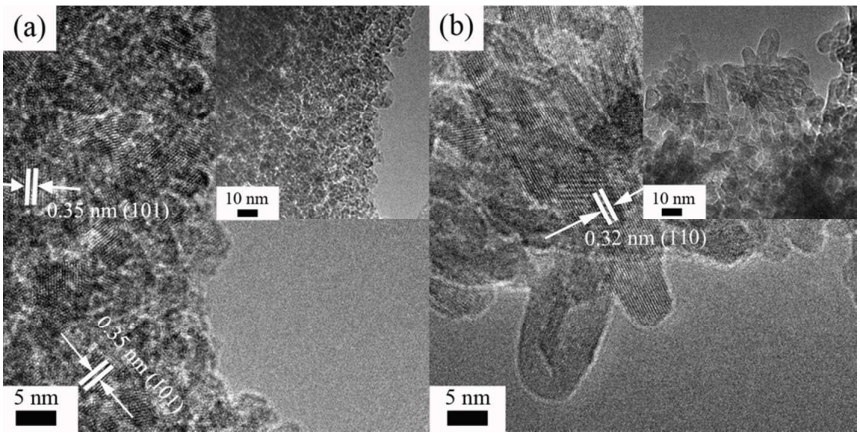

Fig. 11

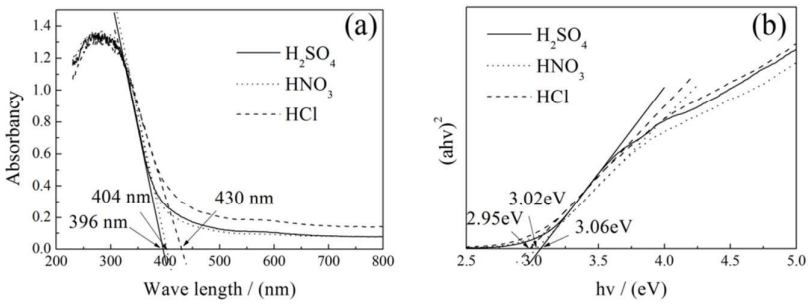

Fig. 12

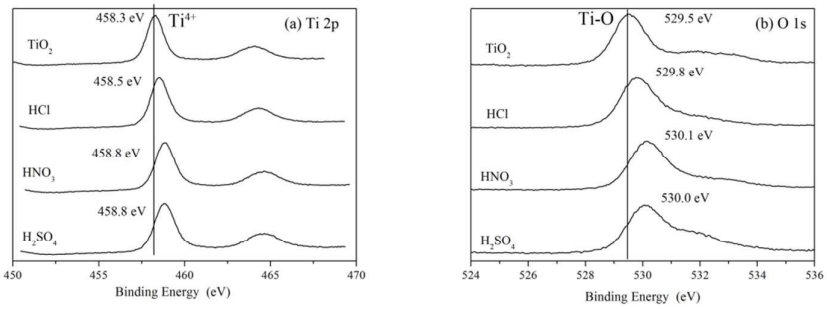

Fig. 13

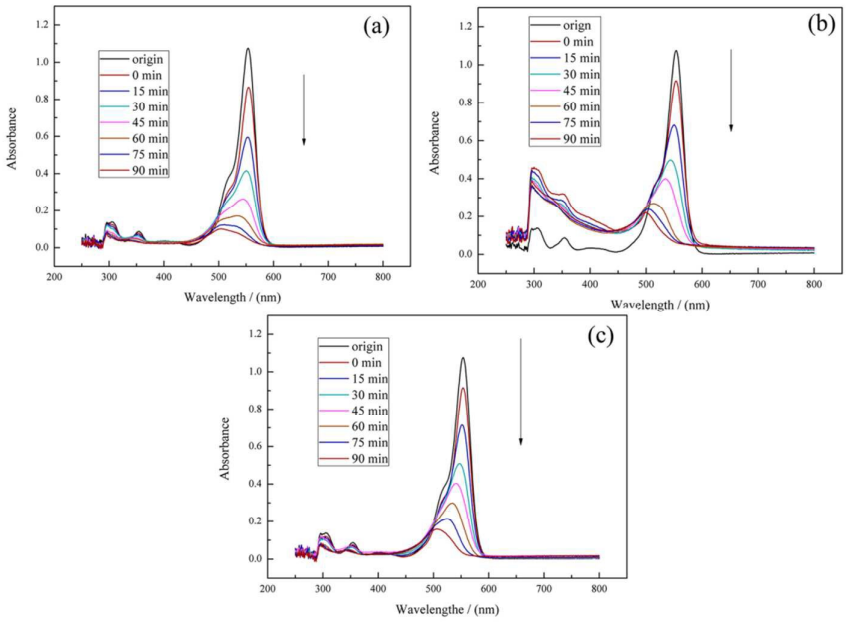

Fig. 14

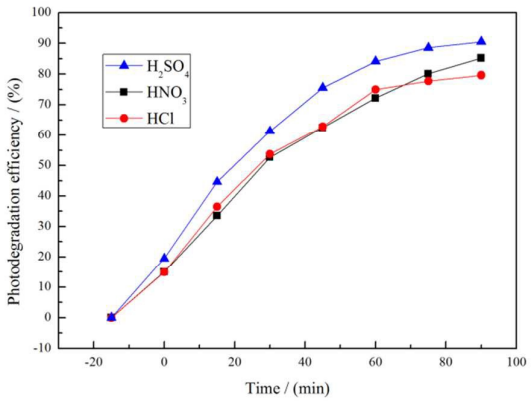

Fig. 15